Towards Advanced Electrochemical Horizon: Ion Selectivity and Energy Harnessing Through Hybrid Capacitive Deionization with Carbon-Coated NaTi$_2$(PO$_4$)$_3$ and N-rich Carbon Nests

Hanieh Sharifpour[a], Farzaneh Hekmat[b,*], Saeed Shahrokhian[a,*], Likun Pan[c]

Table of Contents

S1. EXPERIMENTAL SECTION

S1.1. Chemicals

Ethylene glycol (EG), tetra-butyl titanate (TBOT), monosodium phosphate dehydrates ($NaH_2PO_4 \cdot 2H_2O$), phosphoric acid (H_3PO_4), nickel sulfate hexahydrate ($NiSO_4.6H_2O$), hexamethylenetetramine (HMT), glucose ($C_6H_{12}O_6$), polyvinylidene fluoride (PVDF), dimethylformamide (DMF), sodium chloride (NaCl), calcium chloride ($CaCl_2$), magnesium chloride ($MgCl_2$), and potassium chloride (KCl) are of analytical grade and were obtained from Merck (Germany). Arian Gas (Iran) supplied high-purity argon gas (99.999%) to utilize as inert carrier gas through heat treatment procedures. In addition, hydrochloric acid (HCl, 37%) and acetone (C_3H_6O) were both received from PARS SHIMI Company (Iran). Double−distilled (DI) water (18.2 MΩ), which was utilized for the experiments, attained from a Zolalan water purification system (Iran).

S1.2. Material Characterization

To prepare active materials, hydrothermal procedures were all conducted employing an electric oven, which was obtained from Atra Co. ACE400L-60DH, Iran). Heat-treated processes (e.g. carbonization and annealing) were also carried out using a tube furnace under 99.999% argon gas flow (ATE 1100 L, Atra, Iran). Electrode-active materials were structurally evaluated through different characterization methods. Accordingly, surface morphology and corresponding elemental compositions were investigated using a field-emission scanning electron microscope (FE-SEM) (TESCAN, MIRA III LMU, Czech Republic), integrated with an energy dispersive spectroscopy (EDS). The crystalline structure of the prepared samples was further explored employing an X-ray diffraction (XRD) spectroscopy (RIGAKUD/MAX -

IIIC diffractometer, Bruker, Germany)). Fourier transform infrared (FTIR) spectra of samples were further recorded using a Perkin Elmer FT-IR spectrometer (USA). An XploRA PLUS Raman spectrometer (HORIBA Ltd., Japan) was also employed for further structural characterization of the prepared active materials. Specific surface area (SSA) and pore-size distribution were also investigated according to the Nitrogen adsorption-desorption isotherms, which were achieved by a gas adsorption analyzer (Bel, Belsorp mini II, Japan). Pore size distribution and SSA were calculated from N_2 adsorption data regarding the Barrett-Joyner-Halenda (BJH) and Brunauer-Memmett-Teller (BET) theories, respectively. Chemical composition along with the oxidation states of the surface atoms were further studied using an X-ray photoelectron microscopy (XPS) (ESCALAB 250Xi with an AL X-ray, Thermo Fisher Scientific, Germany). An ARCOS trademark (SPECTRO Analytical Instruments, Germany) inductively coupled plasma optical emission spectrometer (ICP-OES) was used to analyze water quality. A CHN analysis (Perkin Elmer, 2400, USA) was also employed for further investigation about the contribution of the carbon contents of electroactive material.

S1.3. Energy Storage Capacity Evaluation

Electrochemical methods, including cyclic voltammetry (CV), galvanostatic charge/discharge (GCD), and electrochemical impedance spectroscopy (EIS) were used to study the electrochemical performance of supercapacitor electrodes. CVs and GCD measurements were conducted using a potentiostat-galvanostat workstation (Radstat1000, Kianshar Danesh Co., Iran). The electrochemical responses of positive and negative electrodes were both studied in a three-electrode configuration, using a saturated Ag/AgCl reference electrode (Azar Electrode Co., Iran), a 2 cm × 3 cm graphite counter electrode, and a 1 cm × 1 cm × 0.8 cm graphite sheet as a working electrode, where different saline water was used as the electrolyte. EIS measurements were further acquired employing an electrochemical workstation (PGSTAT204,

Autolab, Netherlands) at the open circuit potential (OCP) condition, applying an alternating potential with an amplitude of 5 mV in the frequency range from 100 kHz to 10 mHz.

S1.4. Evaluation of the Desalination Capacity of the Fabricated IEM-HCDI Cells

The electric conductivities were recorded using an Eutech ^{TM} PC 2700 Multi−parameter Meter (Eutech Instruments, Netherland) equipped with a Eutech™ CONSEN9201D conductivity/temperature/pH electrode and an ATC Probe (PH5TEMB01P). A LabF3 peristaltic dispensing pump (SHENCHEN, China) was employed to control the influent stream. The inlet and outlet water quality (the salts concentration in influent/effluent streams) were determined using atomic absorption and emission spectrometers (AAS and AES). The sodium, magnesium, and calcium concentrations were detected employing a Varian Spectra 220 AAS (Australia), and for the potassium concentration, Corning 410 K AES (England) was used.

S1.5. Prototype IEM-HCDI Water Desalination Cells

Two 7.5 cm × 7.5 cm × 0.8 cm graphite sheets were used as current collectors in fabricating the HCDI cells, which were held by two Plexiglas plates as holders. The electrode active materials were then drop-casted onto the graphite substrates from a homogeneous slurry (95% of electrode active material and 5% PVDF in DMF) to prepare positive and negative electrodes. According to the mass balance calculations, 35 mg NTP−C and 45 mg NCNs were coated onto the graphite current collectors and the fabricated electrodes were then dried at 160 °C for 2 h. The prepared NTP-C negative and NCN positive electrodes were next utilized in the HCDI cells. In all experiments, an ion exchange membrane (IEM) was placed between the positive and negative electrodes as a separator. The feasibility of using in flow-by configuration was investigated by evaluating the electrochemical performance of the fabricated IEM-HCDI cells. A complete removal process covers a two-step procedure, including electrosorption and

regeneration steps in sequence, in which each steps last almost 25 min at a 1.5 mL min^{-1} flow rate. A constant potential of 2 V was applied within the electrosorption step to investigate the ion selectivity of the prepared IEM-HCDI cells in a variety of saline water streams. To reveal the practical applicability of the fabricated devices in energy recovery, commercial light-emitting diodes (e.g. red, green, and yellow ones) were lit up with the prepared IEM-HCDI cells. It is worth considering that the polarity was reversed in the regeneration step to not only recover the electrodes but also harvest the generated energy.

S1.6. NTP-C Negative Electrodes Fabrication

Tetra butyl titanate (TBOT) (680.72 µL) was first dropwise added into 20 mL of ethylene glycol (EG) within 30 min under vigorous stirring to obtain a transparent solution. Herein, EG was used as an inhibitor to hinder the hydrolysis of TBOT. The prepared mixture was then labeled as solution A. Another clear solution was then prepared by dissolving $NaH_2PO_4 \cdot 2H_2O$ (1.56 g) into 100 mL of DI water under vigorous stirring. A 10 mL aqueous glucose solution (0.1 M), including H_3PO_4 (104.24 µL) was next added into the prepared monosodium phosphate solution and labeled as solution B. Thereupon the prepared solution was added into solution A under ultrasonication for 10 min more. The obtained mixture was subsequently transferred into a 100 mL Teflon-lined stainless-steel autoclave and kept at 180°C for 12 h. After the due time, the autoclave was cooled down to room temperature and the synthesized precursors were collected and dried at 100°C for 5 h. At the beginning of a time-dependent solvothermal treatment, the carbon-coated NTP hierarchical precursors were first nucleated from an evolution process. As a direct consequence of the directional attachment, the precursors began to agglomerate into interconnected nanosheets. The desired sodium-ion selective NTP−Cs were eventually achieved through the annealing process. Accordingly, the

brown slimy precursors were first preheated at 350°C for 2 h, followed by annealing at 700°C

for 4.5 h under an inert atmosphere (Ar, 99.999%) with a heating rate of 2°C min^{-1}.

S1.7. NCN Positive Electrodes Fabrication

 With a slight modification compared to our previous work, the NCNs were synthesized and

utilized as positive electrode active materials.[3] Nickel sulfate hexahydrate (1.11 g), HMT (0.6

g), and glucose (0.5 g) were first dispersed in 45 mL DI water. The prepared solution was then

stirred magnetically for 15 min to obtain a homogeneous solution. The green-bluish solution

was next transferred into a 100 mL Teflon-lined stainless-steel autoclave and heated at 180 °C

for 24 h. Afterward, the autoclave was cooled down to room temperature, and the precipitates

were filtered and dried at 60 °C overnight. The precursors were finally carbonized at 700 °C

and Ni metallic components were subsequently removed via an acid treatment route by kipping

the products in a 37% HCl solution for 10 h. The prepared NCNs were then washed with DI

water until reaching a neutral pH.

S1.8.   Electrolytes and Feed Water Streams

The energy storage capabilities of positive and negative electrodes were individually explored

in 1M NaCl solution (58440 ppm) through different electrochemical analysis, including CV,

GCD, and EIS. A variety of feed water streams, including different concentrations of NaCl salt

was prepared. The prepared saline solutions with different concentrations, ranging from 100 to

500 ppm were used as the feed water streams in capacitive deionization measurements. The

Na$^+$ selective feature of the fabricated NTP-C electrodes and IEM-HCDI cells was respectively

evaluated in 1M and 500 ppm sodium saline solutions in the coexistence of different counter

anions (e.g. chlorine, nitrate, and sulfate) using CV technique. The sodium-ion selectivity was

further assessed in the coexistence of monovalent and divalent cationic interferences, including K^+, Mg^{2+}, and Ca^{2+}. Accordingly, the selective sodium uptake in 1M mono-cationic saline solutions (e.g. NaCl, NaNO$_3$, and Na$_2$SO$_4$) were compared to bi-cationic saline solutions with 1mM of interference cations (e. g. KCl, MgCl$_2$, and CaCl$_2$) as contamination.

S1.9. Electrochemical Measurements

The electrochemical behavior of both NTP-C negative and NCN positive electrodes was individually explored using, the CV technique. CV measurements were conducted within the potential ranges of -1.90 to +0.35 V and -0.56 to +1.00 V, for the NTP-C negative and NCN positive electrodes, respectively. Besides, CVs were obtained at different potential scan rates, ranging from 1.00 to 100 mV s^{-1}. The specific capacity (C$_s$, C g^{-1}) was calculated from CV curves based on the following equation:

$$C_s = \frac{\int I dV}{m \times v \times \Delta V} \tag{$S1$}$$

GCD measurements of the fabricated electrodes were further carried out under different current densities increasing from 0.5 to 4.5 A g^{-1}. The GCD evaluations were also performed within the potential range of -1.60 to $+0.30$ V and -0.70 up to $+1.42$ V, for NTP$-$C negative and NCN positive electrodes, respectively. The long-term stability of each negative and positive electrode was also evaluated up to 3000 charge/discharge cycles. Regarding the energy storage mechanisms—governed predominantly by either charge separation at the electrode/electrolyte interface or diffusion-controlled redox reactions), the specific capacitance (C$_s$, F g^{-1}) or specific capacity (Q, C g^{-1}) of each negative and positive electrode was calculated from the following equations, respectively. [1-4]

$$Q = \frac{i \int dt}{m \times \Delta V} \tag{S2}$$

where i is the applied current (A), m (g) is the mass loading of electrode active materials, and ΔV is the potential window obtained from GCD measurements. [1,2]

$$C_s = \frac{I \times \Delta t}{m \times \Delta V} \tag{S3}$$

where I (A), Δt (s), m (g), v (mV s^{-1}), and ΔV (V) are the current, discharge time, mass loading of electrode active material, potential scan rate, and operating potential window. [3,4]

The electrochemical behavior of the fabricated NTP-C//NCN asymmetric devices was further evaluated. It is worth considering that the assembled CDI cells can render neither remarkable capacitive deionization performance nor high energy storage behavior unless the mass balance between the NCN positive and NTP-C negative electrodes obeys the following rule: [5]

$$\frac{m^+}{m^-} = \frac{C_{sp}^- \times \Delta V^-}{C_{sp}^+ \times \Delta V^+} \tag{S4}$$

, here, the C_{sp}^-, C_{sp}^+ were calculated from the CV measurements in 3-electrode configurations, ΔV^-, ΔV^+ are the positive and negative electrodes' operating potential windows, and m^+, m^- were assigned to the mass of each positive and negative electrode, respectively.

The specific capacity Q (C g^{-1}) of the assembled asymmetric device was further estimated from the GCD curves according to the following equation:

$$Q_{cell} = \frac{i \int dt}{M \times \Delta V} \qquad ; M = m_1 + m_2 \tag{S5}$$

, in which the gravimetric capacity of the cell (C g^{-1}), discharge current (A), and discharge time (s) are shown by Q_{cell}, I, and t, respectively. The total mass loaded of negative and positive active materials is also presented by M.
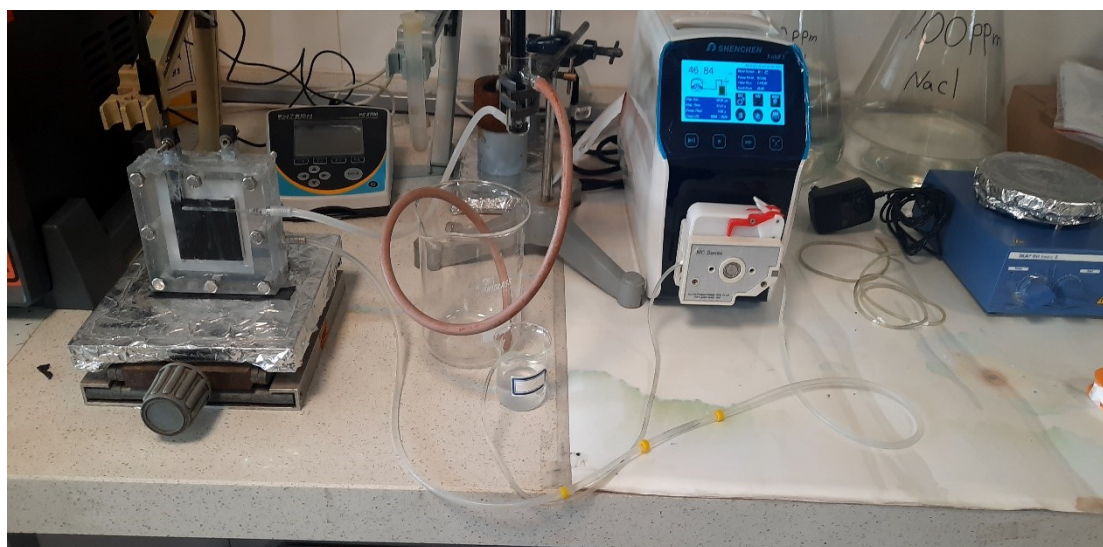
S2. Supplementary Figures and Tables

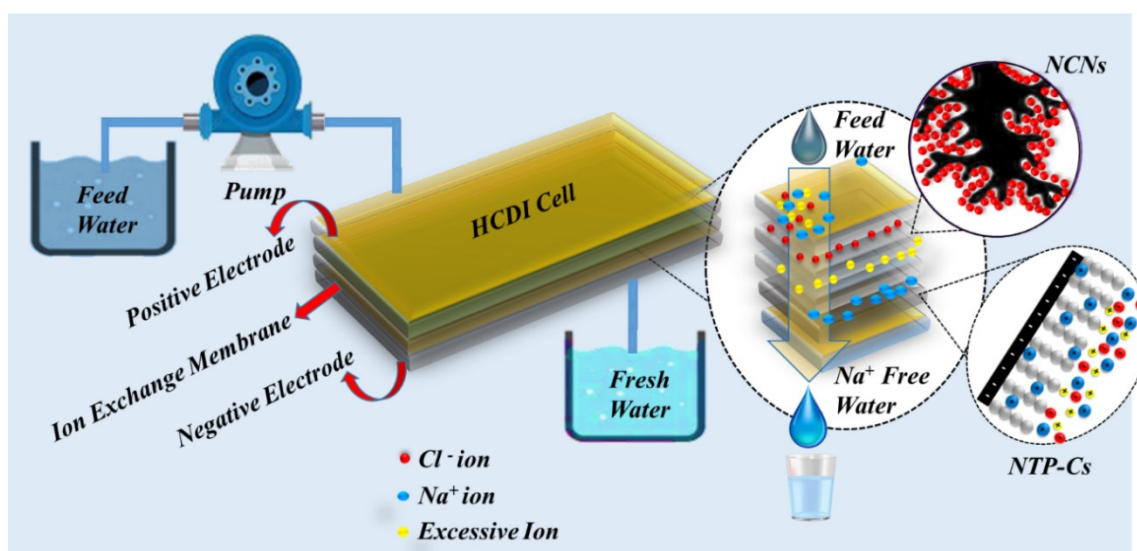**Fig. S1** The fabricated lab-scale NTP-C//NCN IEM-HCDI unit.

Fig. S2 Graphical description of the inner chamber through a sodium selective desalination by NTP−C intercalative anode and NCN capacitive cathode in an HCDI process.

Table S1. Distribution of O, Ti, C, P, and Na elements of the prepared NTPs and NTP−Cs, obtained from the elemental EDX analysis (before post-annealing (BPA) and after post-annealing (APA)).

Element (wt%)	O	Ti	C	P	Na
NTP(BPA)	45.36	20.14	2.66	25.73	5.65
NTP-C(BPA)	46.47	15.46	14.36	19.97	3.14
NTP-C(APA)	41.55	23.80	16.61	16.46	1.59

BPA: before post-annealing, APA: after post-annealing

Table S2. The C contents (%) distribution from CHN results for the as-prepared NTP and NTP−C material.

Material	NTPs	NTP−Cs
C %	5.05	12.26
H%	1.62	3.29
N%	–	–

S2.1. Supplementary Notes for RAMAN Analysis

As seen in Figure S3A and B, observation of two prominent peaks at the wavenumbers ranging from 1300-1400 and 1500-1600 cm^{-1}, known as D and G bands, provide clear evidence of the successful synthesis of carbon-embedded structures. When compared to the G-bands, originating from in-plane vibrations, the intensity of D-bands reflects the lattice disorders, mainly resulting from amorphous carbons. Being extremely impressed by symmetry-breaking

disorders, Raman spectroscopy is a powerful technique commonly used for exploring the degree of crystallinity in carbons[6] the intensity ratio of the D to G band (I_D/I_G ratio), in this regard, is immensely valuable in exploring the disorder incorporation in carbon materials. As seen in the figures, the I_D/I_G ratio was obtained almost over 0.80 for both NTP−C and NCN active materials. These relatively high-intensity ratios can be attributed to the high graphitization degree of both electrode materials, which can guarantee their remarkable electric conductivity.[7-9]
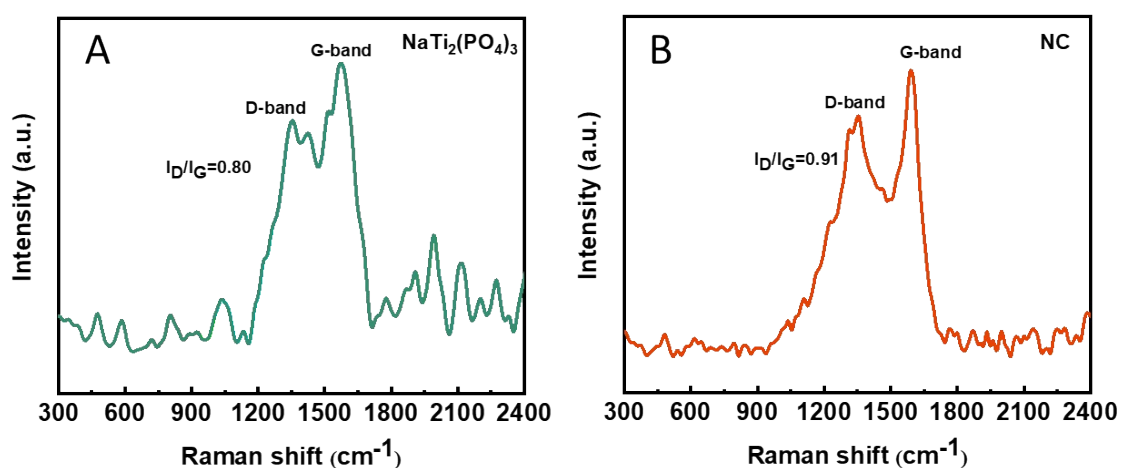
Fig. S3 Characterization of the prepared electrode materials. (A, B) Raman spectra of the NTP−Cs and NCNs, respectively.

S2.2. Supplementary Notes for Nitrogen Adsorption–Desorption Isotherms

Taking a leading part in not merely charge storage but also water desalination, both SSA and pore size distribution are of prime significance in fabricating high-performance electrochemical devices. Establishing a similarity between the obtained isotherms type IV_a of the IUPAC calcification, NTP-Cs, and NCNs (Figure S4A and B, respectively) both gain advantages from mesoporous nanostructures, which can assure their strain relaxation, volume change accommodation, and rapid Na^+ and X^- diffusion.[8, 10, 11] Regarding the BET theory, the

SSA of NTP−Cs and NCNs was measured to be 52.4 and 1367.9 m^2g^{-1}, respectively. The average pore diameter of the prepared NTP-Cs and NCNs was further estimated according to the BJH curves, provided in Figure S4A and B (inset). In total agreement with type N_2 adsorption/desorption isotherms, both NTP-C and NCN electrode materials benefit from mesoporous nanostructures with a large pore diameter of 30 and 1 nm, respectively.
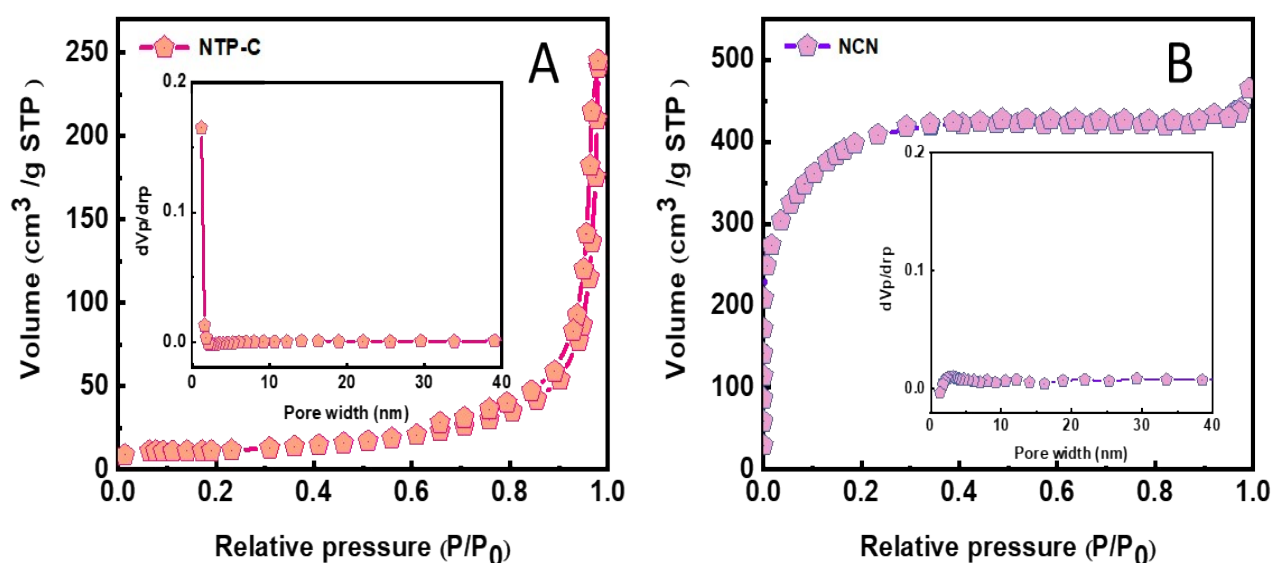

Fig. S4 Nitrogen adsorption-desorption isotherms with the corresponding BJH pore size distribution plot in the inset.

Table S3. Conductivity parameters of different electrolytes (1M of NaCl, Na_2SO_4, $NaNO_3$, KCl, $CaCl_2$, and $MgCl_2$)

Electrolytes	Ionic conductivity (mS)
NaCl	86.64
Na_2SO_4	95.37
$NaNO_3$	76.57
KCl	111.32

CaCl_2	129.51
MgCl_2	87.67

Table S4. Hydrated size and the hydration energy of different cations.[12-14]

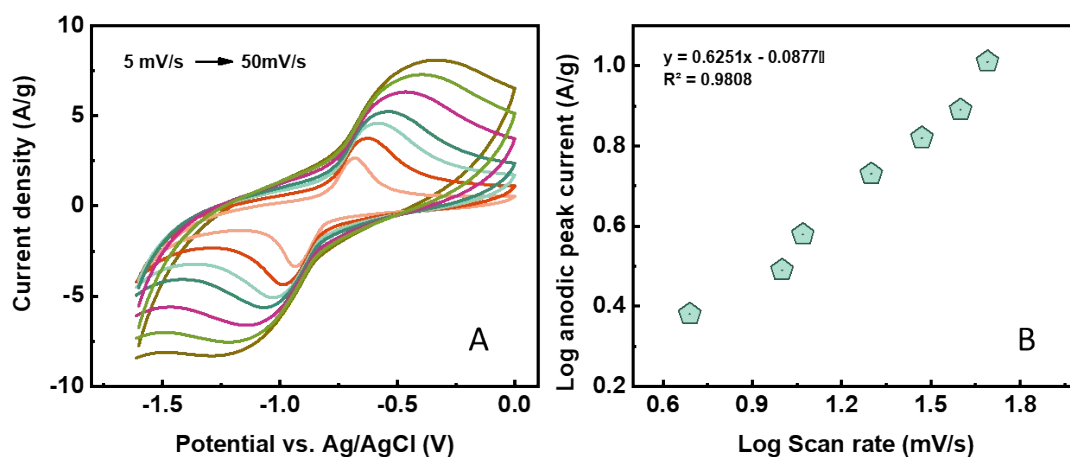| Ion	Hydrated ion size (nm)	Hydration free energy ((KJ mol^{-1}))
Na^+	0.358	-405
K^+	0.331	-321
Ca^{2+}	0.412	-1592
Mg^{2+}	0.428	-1922
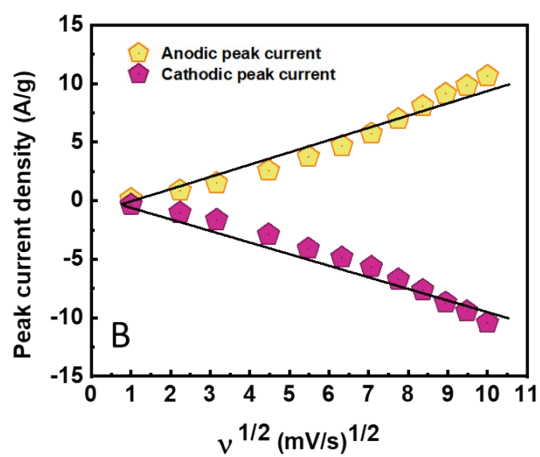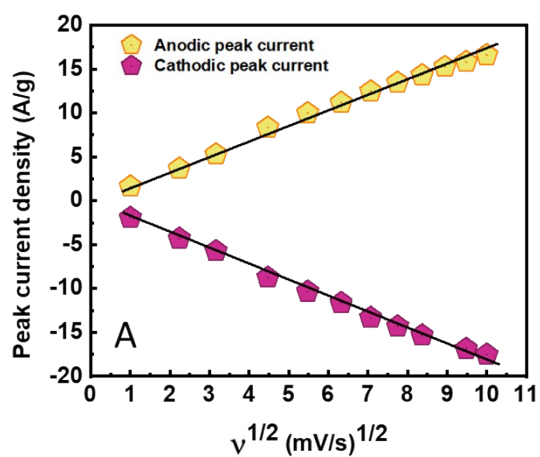
Fig. S6 A) CVs of the NTP electrodes at different potential scan rates and corresponding B) variation of the logarithmic amount of the anodic peak current density and potential scan rates.

Electrode	R_s ($\Omega.\ cm^2$)	CPE_{dl} ($mF.cm^2\ S^{P-1}$)	R_{ct} ($\Omega.cm^2$)	P	CPE_f ($mF.cm^2\ S^{P-1}$)	R_l (Ω)	W ($\Omega.\ cm^2$)	Chi-squared
NTP−C	2.93	416	1.16	0.63	-	-	787.4	0.00044
NC	4.43	351	0.022	0.68	99	1.4	5.72	0.00041

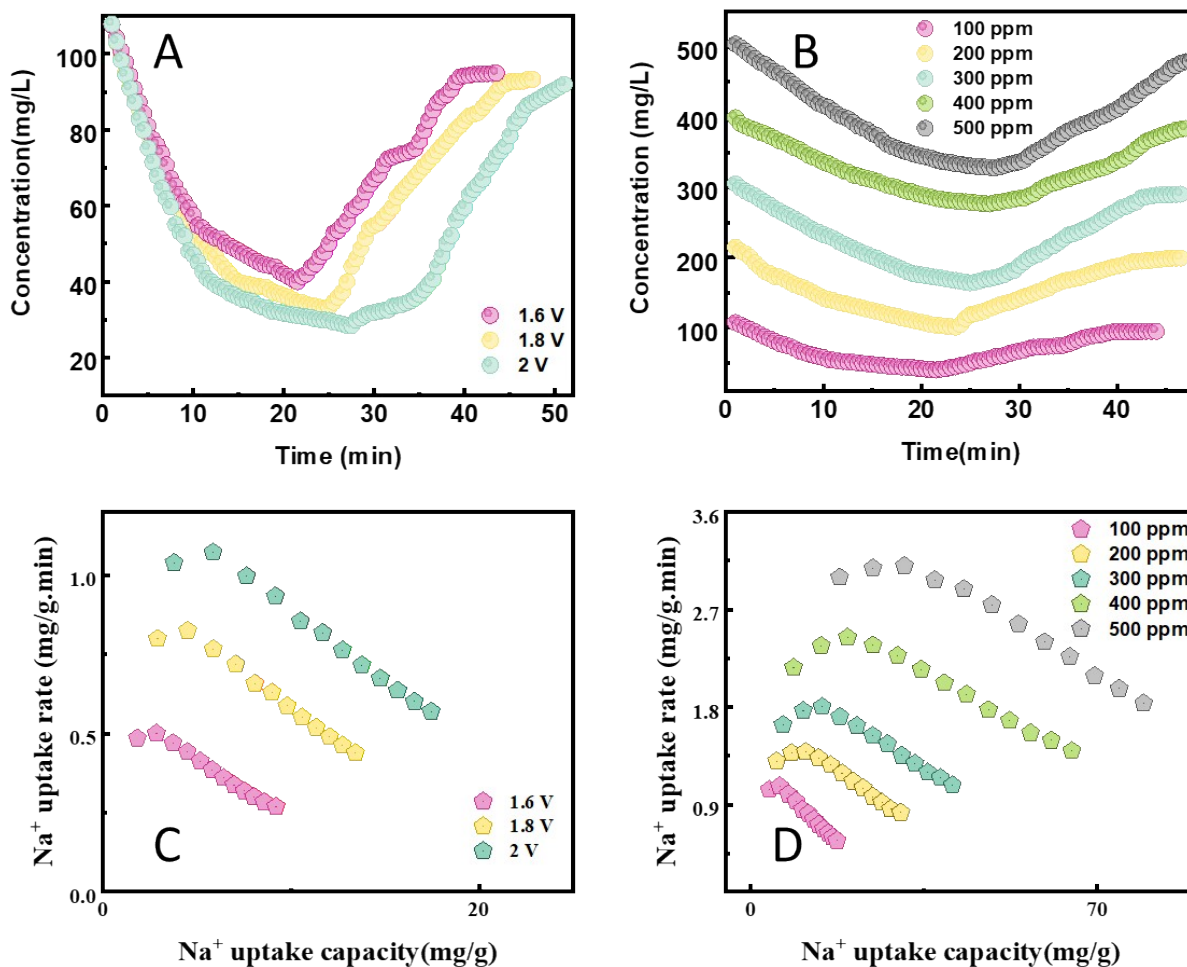**Table S5.** The calculated EIS parameters.

Fig. S7 A) Effect of applied cell potential (1.6, 1.8, and 2 V) in a 500 ppm of NaCl solution and B) different concentrations of 100, 200, 300, 400 and 500 ppm of NaCl solutions during NTP−C//NCN HCDI removal process, sodium adsorption capacity versus sodium adsorption rate (CDI Ragone plots) C) under different applied potential of 1.6, 1.8 and 2 V and D) in different concentrations of NaCl at 2 V.
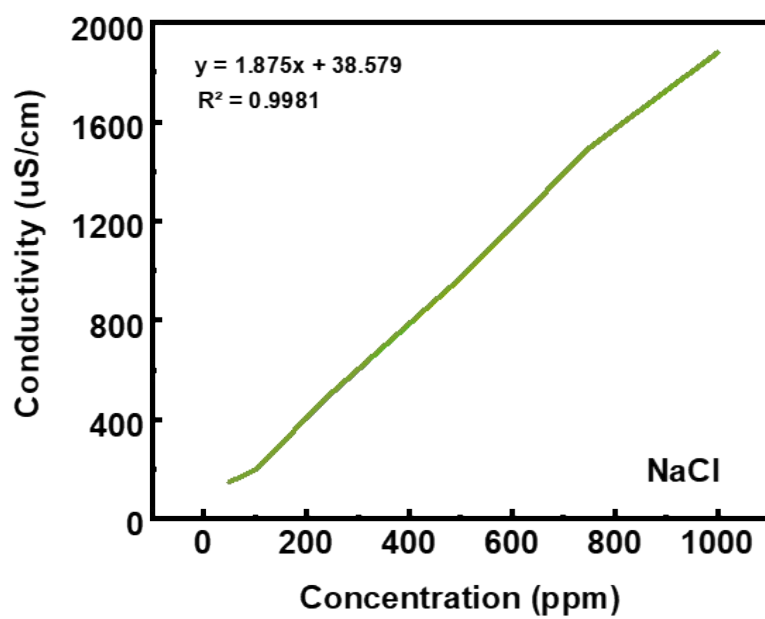
Fig. S8 The conductivity–concentration calibration curve in different concentrations of NaCl solutions.
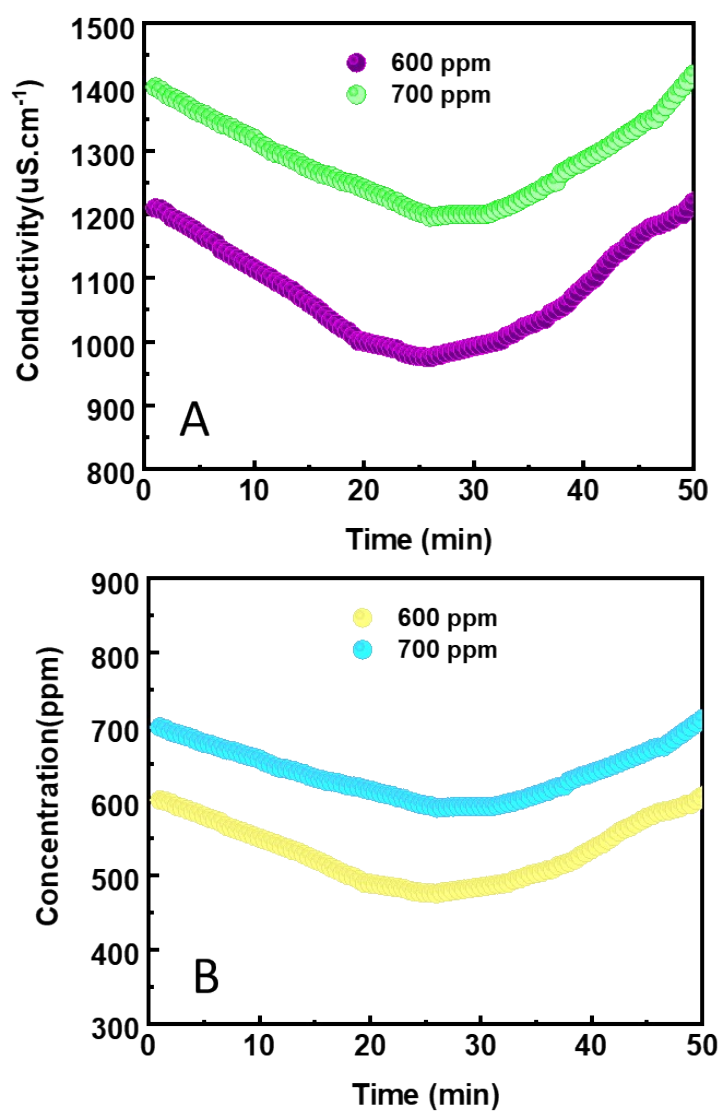
Fig. S9 A) The conductivity and B) the concentration profiles for 600 and 700 ppm of NaCl solutions during the ion-removal process obtained using NTP-C//NCN IEM-HCDI cells.

Table S6. Evaluated SAC, SAR, and SRE% for 600 and 700 ppm of NaCl solutions.

Concentration	SAC (mg g⁻¹)	SAR (mg g⁻¹ min⁻¹)	SRE %
600ppm	115.71	4.13	20.14
700 ppm	144.57	5.16	15.27

S2.3. Supplementary Notes for pH profile during one adsorption-desorption cycle

The pH profile of the effluent was explored during the adsorption-desorption process. No need to say that a pure 100-500 ppm NaCl solution — which was prepared using double distilled water and highly pure dried sodium chloride salt, was used as the effluent stream in the current research. According to the negligible total changes of 0.8 (at the highest voltage of 2 V) in recorded pH (Fig. S10) at a constant temperature of 24-24.5 ^oC, it was confirmed that water decomposition did not occur up to 2 V. The initial pH of the feed water was approximately 6.22, which reached 6.85 at the adsorption branch, then decreased at the desorption to 5.85 and increased following to a constant value of 6.08 which was lower than the initial pH. During the adsorption step, the effluent pH is higher than the feed pH, whereas, during desorption, the effluent pH is lower than the feed pH. Our study predicted only minor pH changes during desalination when non-Faradaic processes, including the effect of different mobilities combined and the presence of chemical surface groups in the micropores, are taken into account[15-17]. At the beginning of the adsorption step, a slight increase in effluent pH was attributed to the different removal rates of OH^- and H^+ ions, not by electrode reactions. The ionic mobility of the H+ ion (3.63×10^{-3} cm^2 s^{-1} V^{-1}) is approximately 1.8 times higher than that of the OH^- ion ($2.05 \times \times 10^{-3}$ cm^2 s^{-1} V^{-1})[18]. It is thought that the removal rate of H^+ ions is higher than that of OH- ions during adsorption, increasing effluent pH. In addition, undesirable reactions also occur. These Faradaic processes must be considered predicted to be a protonation or deprotonation of chemical surface groups present on the electrode material, which can also result in pH changes during CDI operation.[16,17] Experimentally and theoretically, many studies have reported the same pH profiles during desorption if the feed water only contains sodium chloride.
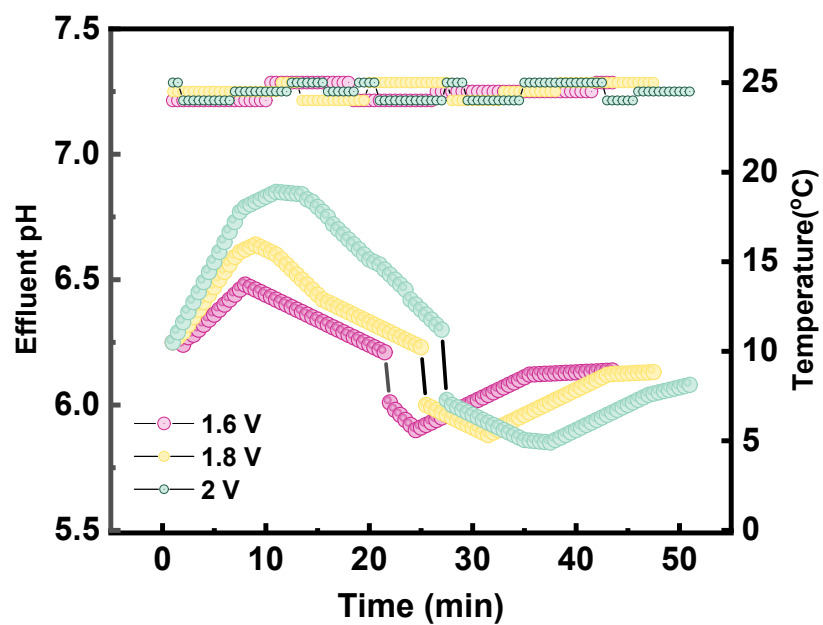
Fig. S10. pH variation during one adsorption-desorption cycle at different applied cell potentials (1.6, 1.8, and 2 V) in a 500 ppm of NaCl solution.
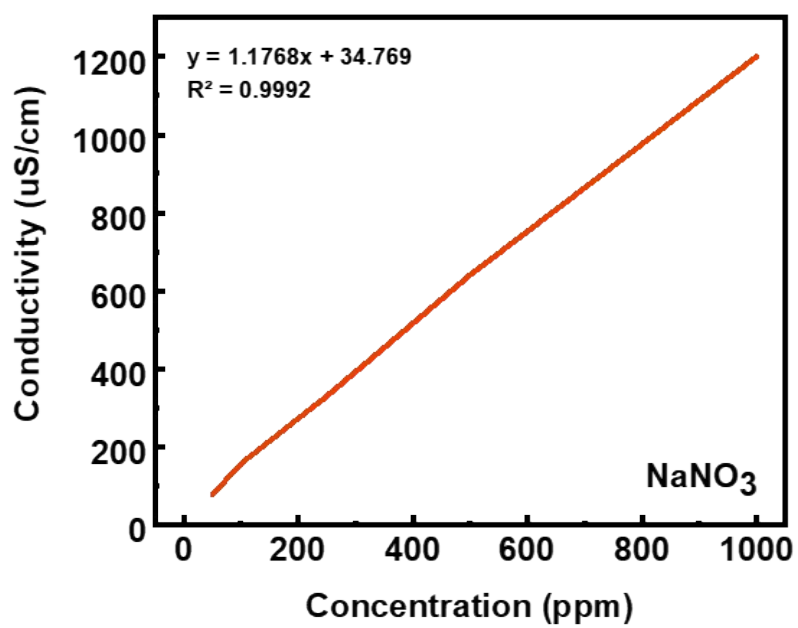
Fig. S11 The conductivity–concentration calibration curve in different concentrations of $NaNO_3$ solutions.
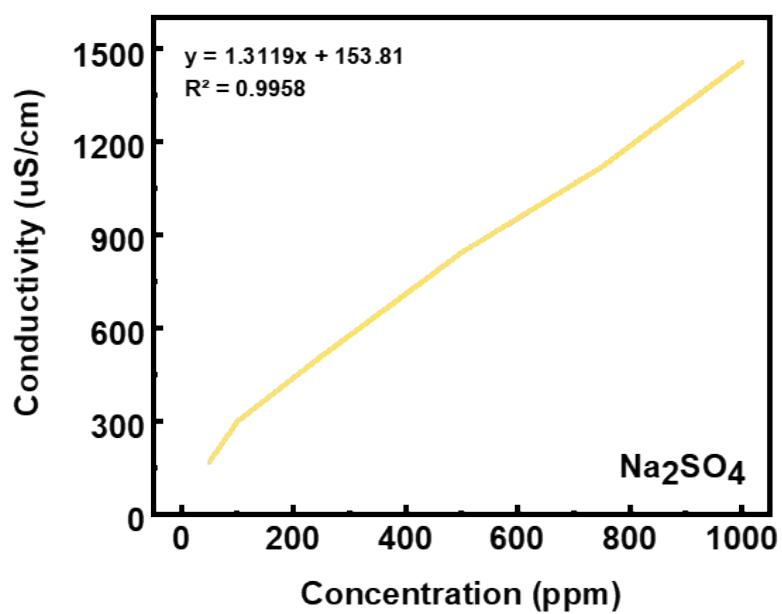
Fig. S12 The conductivity–concentration calibration curve in different concentrations of Na_2SO_4 solutions.

S3. References

(1) Hosseini, H.; Shahrokhian, S. Self-Supported Nanoporous Zn–Ni–Co/Cu Selenides Microball Arrays for Hybrid Energy Storage and Electrocatalytic Water/Urea Splitting. *J. Chem. Eng.* **2019**, *375*, 122090.

(2) Shahi, M.; Hekmat, F.; Shahrokhian, S. Hybrid Supercapacitors Constructed from Double-Shelled Cobalt-Zinc Sulfide/Copper Oxide Nanoarrays and Ferrous Sulfide/Graphene Oxide Nanostructures. *J. Colloid Interface Sci* **2021**, *585*, 750-763.

(3) Huang, J.; Xie, Y.; You, Y.; Yuan, J.; Xu, Q.; Xie, H.; Chen, Y. Rational Design of Electrode Materials for Advanced Supercapacitors: from Lab Research to Commercialization. *Adv. Funct. Mater.* **2023**, *33* (14), 2213095.

(4) Sharifpour, H.; Hekmat, F.; Shahrokhian, S. Unraveling the Ion Uptake Capacitive Deionization of Sea-and Highly Saline-Water by Sulfur and Nitrogen Co-Doped Porous Carbon Modified with Molybdenum Sulfide. *ACS Appl. Mater. Interface* **2023**, *15* (36), 42568-42584.

(5) Hekmat, F.; Shahrokhian, S.; Rahimi, S. 3D Flower-Like Binary Nickel Cobalt Oxide Decorated Coiled Carbon Nanotubes Directly Grown on Nickel Nanocones and Binder-Free Hydrothermal Carbons for Advanced Asymmetric Supercapacitors. *Nanoscale* **2019**, *11* (6), 2901-2915.

(6) Wang, K.; Liu, Y.; Ding, Z.; Li, Y.; Lu, T.; Pan, L. Metal–Organic-Frameworks-Derived NaTi 2 (PO 4) 3/Carbon Composites for Efficient Hybrid Capacitive Deionization. *J. Mater. Chem. A* **2019**, *7* (19), 12126-12133.

(7) Xu, Y.; Cao, W.; Yin, Y.; Sheng, J.; An, Q.; Wei, Q.; Yang, W.; Mai, L. Novel NaTi2 (PO4) 3 Nanowire Clusters as High Performance Cathodes for Mg-Na Hybrid-Ion Batteries. Nano Energy **2019**, 55, 526-533.

(8) Xu, C.; Xu, Y.; Tang, C.; Wei, Q.; Meng, J.; Huang, L.; Zhou, L.; Zhang, G.; He, L.; Mai, L. Carbon-Coated Hierarchical NaTi2 (PO4) 3 Mesoporous Microflowers with Superior Sodium Storage Performance. *Nano Energy* **2016**, *28*, 224-231.

(9) Huang, Y.; Chen, F.; Guo, L.; Yang, H. Y. Ultrahigh Performance of a Novel Electrochemical Deionization System Based on a NaTi 2 (PO4)3/rGO Nanocomposite. *J. Mater. Chem. A* **2017**, *5* (34), 18157-18165.

(10) Traškina, N. d.; Gečė, G.; Pilipavičius, J.; Vilčiauskas, L. Polydopamine Derived NaTi2 (PO4) 3–Carbon Core–Shell Nanostructures for Aqueous Batteries and Deionization Cells. *ACS Appl. Nano Mater* **2023**, *6* (13), 11780-11787.

(11) Wang, Z.; Ma, Q.; Wang, L.; Gong, X.; Jia, D.; Luo, Y.; Guo, N.; Ai, L.; Xu, M. Porous NaTi2 (PO4) 3 Nanoparticles Encapsulated in Nitrogen-Doped Carbon Matrix for High-Performance Capacitive Deionization. *ACS Sustain Chem Eng* **2023**, *11* (40), 14701-14709.

(12) Volkov, A.; Paula, S.; Deamer, D. Two mechanisms of permeation of small neutral molecules and hydrated ions across phospholipid bilayers. *Bioelectrochemistry and bioenergetics* **1997**, 42 (2), 153-160.

(13) Nightingale Jr, E. Phenomenological theory of ion solvation. Effective radii of hydrated ions. *The Journal of Physical Chemistry* **1959**, *63* (9), 1381-1387.

(14) Tansel, B. Significance of thermodynamic and physical characteristics on permeation of ions during membrane separation: Hydrated radius, hydration free energy and viscous effects. *Separation and purification technology* **2012**, 86, 119-126.

(15) A. Hassanvand, G.Q. Chen, P.A. Webley, S.E. Kentish, A comparison of multicomponent electrosorption in capacitive deionization and membrane capacitive deionization, *Water research*, 131 (**2018**) 100-109.

(16) W. Tang, D. He, C. Zhang, P. Kovalsky, T.D. Waite, Comparison of Faradaic reactions in capacitive deionization (CDI) and membrane capacitive deionization (MCDI) water treatment processes, *Water research*, 120 (**2017**) 229-237.

(17) A.C. Arulrajan, J.E. Dykstra, A. Van Der Wal, S. Porada, Unravelling pH changes in electrochemical desalination with capacitive deionization, *Environmental Science & Technology*, 55 (**2021**) 14165-14172.

(18) C. Wang, L.-F. Ren, D. Ying, J. Jia, J. Shao, Enhancing performance of capacitive deionization under high voltage by suppressing anode oxidation using a novel membrane coating electrode, *Journal of Membrane Science*, 652 (**2022**) 120506.